Robustness of topological surface states against strong disorder observed in Bi_2Te_3 nanotubes

Renzhong Du,[1,2] Hsiu-Chuan Hsu,[1] Ajit C. Balram,[1] Yuewei Yin,[1] Sining Dong,[3] Wenqing Dai,[1] Weiwei Zhao,[1,2] DukSoo Kim,[2,4] Shih-Ying Yu,[2,5] Jian Wang,[1,2,6] Xiaoguang Li,[3] Suzanne E. Mohney,[2,5] Srinivas Tadigadapa,[2,4] Nitin Samarth,[1,2] Moses H. W. Chan,[1,2] Jainendra. K. Jain,[1] Chao-Xing Liu,[1,2] and Qi Li[1,2]

[1]*Department of Physics, Pennsylvania State University, University Park, Pennsylvania 16802, USA*

[2]*Center for Nanoscale Science, Pennsylvania State University, University Park, Pennsylvania 16802, USA*

[3]*Hefei National Laboratory for Physical Sciences at Microscale, Department of Physics, University of Science and Technology of China, Hefei 230026, China*

[4]*Department of Electrical Engineering, Pennsylvania State University, University Park, Pennsylvania 16802, USA*

[5]*Department of Materials Science and Engineering, Pennsylvania State University, University Park, Pennsylvania 16802, USA*

[6]*International Center for Quantum Materials, School of Physics, Peking University, Beijing 100871, China*

(Received 3 September 2015; revised manuscript received 4 March 2016; published 2 May 2016)

Three-dimensional topological insulators are characterized by Dirac-like conducting surface states, the existence of which has been confirmed in relatively clean metallic samples by angle-resolved photoemission spectroscopy, as well as by anomalous Aharonov-Bohm oscillations in the magnetoresistance of nanoribbons. However, a fundamental aspect of these surface states, namely, their robustness to time-reversal-invariant disorder, has remained relatively untested. In this work, we have synthesized thin nanotubes of Bi_2Te_3 with extremely insulating bulk at low temperatures due to disorder. Nonetheless, the magnetoresistance exhibits quantum oscillations as a function of the magnetic field along the axis of the nanotubes, with a period determined by the cross-sectional area of the outer surface. Detailed numerical simulations based on a recursive Green function method support that the resistance oscillations are arising from the topological surface states which have substantially longer localization length than that of other nontopological states. This observation demonstrates coherent transport at the surface even for highly disordered samples, thus providing a direct confirmation of the inherently topological character of surface states. The result also demonstrates a viable route for revealing the properties of topological states by suppressing the bulk conduction using disorder.

DOI: 10.1103/PhysRevB.93.195402

I. INTRODUCTION

Topological insulators (TIs) are bulk insulators with unusual gapless metallic surface states protected by time reversal symmetry [1–3]. The topological surface states are expected to yield unique phenomena, such as spin-momentum locking and the suppression of nonmagnetic backscattering. Bi_2Se_3 and Bi_2Te_3 are among the most studied three-dimensional (3D) topological insulators, and their surface states have been directly confirmed by angle-resolved photoemission spectroscopy (ARPES) [4,5]. However, signatures of topological surface states in electrical transport are complicated by the fact that the samples often have dominating conduction from bulk channels due to a high density of carriers from impurity states. One way to enhance the surface contribution is to increase the surface-to-volume ratio by reducing the sample size down to the nanometer scale. Experimental studies along this direction have been carried out in Bi_2Se_3 nanoribbons [6–8] and Bi_2Te_3 nanowires [9]. Another possible strategy, which forms the basis of this work, is to increase the disorder in nanoscale samples. Sufficiently strong disorder might be expected to suppress bulk transport, while topological surface states remain immune. However, such robustness has not yet been unambiguously tested experimentally, given that previous results were all conducted in relatively clean samples with a metallic behavior. Here, we report on transport studies of topological insulator Bi_2Te_3 nanotubes that have a larger surface-to-volume ratio than nanowires, and, more importantly for this work, are also much more resistive due to strong disorder. In spite of the insulating bulk at low temperatures, we observe quantum oscillations in the conductance with a period consistent with that expected from conducting surface states. The observation of the Aharonov-Bohm-like oscillations [10,11] in these highly disordered nanotubes provides unambiguous demonstration of the fundamentally topological nature of surface states. Detailed numerical simulations provide important insights into these observations: principally, we find that the localization length of topological surface states is substantially longer than that of other nontopological states, and therefore there is a range of parameters where transport through the bulk is suppressed while that through the topological surface states is not. Our simulations also explain why the oscillations are broad and why their amplitude decays with increasing magnetic fields.

II. SAMPLE PREPARATION AND EXPERIMENTAL METHOD

The Bi_2Te_3 nanotubes were grown by a solution phase method, which has been described elsewhere [12]. Briefly, single-crystal tellurium nanowires were first grown by wet chemical synthesis by reducing TeO_2.$Bi(NO_3)_3$ as a precursor was added into the solution. Nanotubes with an inner hollow structure were then formed through the Kirkendall effect [13,14]. The formation of the nanotube starts from the nucleation sites of bismuth on the surface of tellurium nanowires at different positions. This makes the nanotube wall constituent with multiple single-crystalline facets. Transmission electron microscopy (TEM) and field emission scanning electron microscopy (FESEM) studies confirm the nanotube structure,

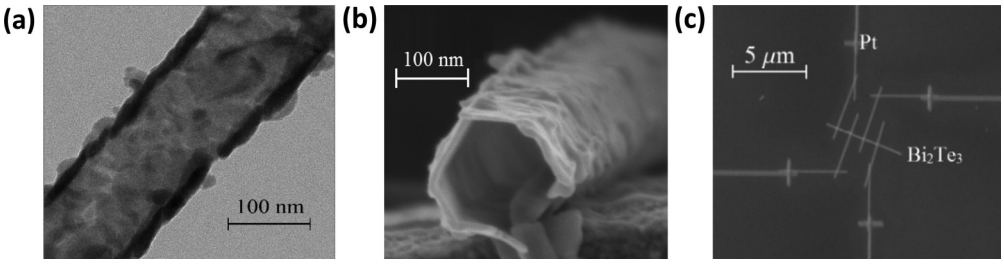

FIG. 1. Microscope images of Bi_2Te_3 nanotube samples. (a),(b) TEM and FESEM images of typical Bi_2Te_3 nanotubes. The TEM image (a) shows the wall thickness. The SEM image (b) shows a cross-section view of a nanotube, with hexagonal cross-section area and empty hollow center. (c) Platinum contacts fabricated on a nanotube by FIB with a four-contact geometry for transport measurements.

as shown in Figs. 1(a) and 1(b). Both SEM and TEM studies of the nanotubes show the typical facet size to be 10–50 nm.

To conduct transport measurements, the Bi_2Te_3 nanotubes were separated from the original reaction solution and dispersed into isopropyl alcohol. They were then dropped onto SiO_2(300 nm)/Si(500 um) substrates before making electrical contacts. Platinum contact leads were fabricated by focused ion beam (FIB) assisted deposition as shown in Fig. 1(c). All measurements were conducted at temperatures down to 1.8 K and high magnetic fields up to 9 T in a Quantum Design physical properties measurement system (PPMS). DC electrical measurements were performed using Keithley 6220 precision current source and 2182 nanovoltmeter with low current and long-time data sampling, as current is driven along the nanotube axis direction. The Seebeck coefficient of single nanotubes was also measured using a micromachined thermoelectric workbench [15] designed for thermal transport measurement of nanowires, in order to obtain supplementary information about the nanotubes.

We report measurements on two nanotubes: nanotube A has an average outer diameter of 125 nm with maximum variation of about 10 nm, and average wall thickness of 13 nm; nanotube B has similar wall thickness, but a smaller average outer diameter of 95 nm. Both nanotubes are about 10 μm long. The FESEM shows that both nanotubes have a measured channel length (the distance between the two voltage leads) of around 700 nm. The small single-crystal grain size (10–50 nm) results in a short electron mean free path due to scattering at grain boundaries. The electron mean free path is further limited by the wall thickness of the nanotubes and additional disorder which is introduced during the FIB processing steps for making electrical contacts. All these characteristics result in samples with much stronger disorder than that observed in other forms of Bi_2Te_3 samples [9,16–18].

III. EXPERIMENTAL RESULTS

A. Temperature dependence of resistance

The temperature dependence of the resistance for nanotube A is shown in Fig. 2. The resistance of the nanotube increases rapidly with decreasing temperature at low temperatures. The carrier type and concentration of the nanotubes were obtained from the Seebeck coefficient measurement on a single nanotube. The carriers are determined as p type and the carrier concentration is estimated to be 5.7×10^{18} cm^{-3} using a relaxation approximation [19]. The carrier concentration value is similar to that reported for thin films and single-crystal samples [20–23] in which metallic behavior is typically observed. However, our nanotube samples are clearly insulating, with a huge increase in resistance with decreasing temperature. The insulating behavior is also shown in the conductance as a function of temperature in the inset of Fig. 2. The rapid increase of resistance with decreasing temperature is in stark contrast to the behavior reported previously in either metallic or semiconducting samples with shallow impurity gaps, even though the carrier concentration of the nanotube has a similar value [20–23]. This demonstrates that the charge carriers in the bulk of the nanotubes are frozen, unlike those in thin films and nanoribbons [6–9,20,24]. The temperature dependence of the nanotube resistance does not fit the standard behavior of either the intrinsic band conduction model or the impurity band conduction model in a semiconductor [24]. Instead, the conductance is well described by Mott variable range hopping (VRH) [25–27] plus a constant for the temperature range above 50 K, $G(T) = G_C + G_0\exp[-(T/T_0)^{-1/(d+1)}]$, as seen in the inset of Fig. 2 (see the Discussion section below for detailed explanations and analysis of the fitting parameters). The fitting suggests two conducting channels in the sample:

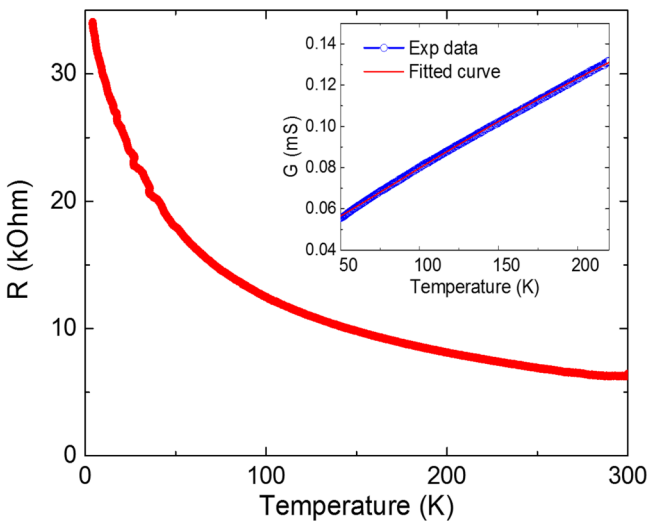

FIG. 2. Resistance as a function of temperature for the nanotube A. It shows a monotonic increase with decreasing temperature, indicating an insulating behavior. Inset: The temperature dependence of conductance. The solid line is a fitting curve using the Mott variable range hopping model plus a constant.

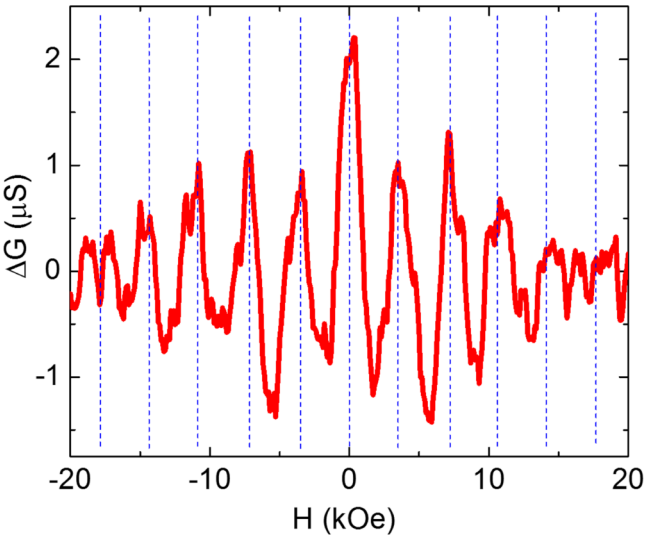

FIG. 3. Magnetoconductance oscillations of the nanotube A (background subtracted) at temperature 1.8 K. Magnetic field is applied parallel to the nanotube axis. The observed period is 3.53 ± 0.20 kOe. This period is consistent with h/e oscillations associated with the outer surface of the nanotube which has an average diameter of 125 nm.

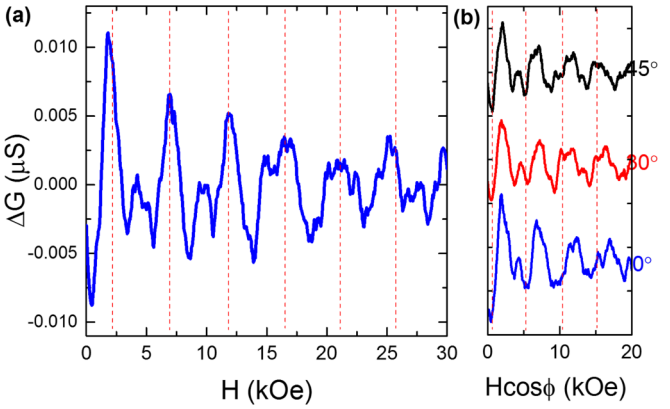

FIG. 4. Magnetoconductance oscillations of the nanotube B (background subtracted) at temperature 2.1 K. (a) Conductance oscillations for the nanotube B. The oscillations show an h/e period associated with the outer surface of the nanotube with a diameter of 95 nm. (b) Conductance oscillations for different magnetic field directions, plotted as a function of the parallel component of the applied field. Evidently, the period depends solely on the parallel component of the applied field.

one is governed by VRH, while the other produces nearly temperature-independent transport. We attribute the former to bulk transport and the latter to the surface transport. The bulk of the nanotube is in the strong-disorder regime, with an extremely short localization length on the order of 1–10 nm (see the Discussion section). This leads to a truly insulating bulk, leaving surface states to dominate the transport at low temperatures. Notably, the surface conductance has a value close to one conductance quantum e^2/h.

B. Magnetoconductance oscillations

Figures 3 and 4(a) show the magnetoconductance (with a smooth background subtracted) of the two nanotubes A and B, respectively, for an external magnetic field applied along the nanotube axis. Conductance oscillations are observed with a period of 3.53 ± 0.20 kOe for the nanotube A and 4.69 ± 0.25 kOe for the nanotube B. The amplitude of the oscillations decays when the magnetic field is increased, but more than seven oscillation periods can be resolved up to 30 kOe for both nanotubes. The angular dependence of the magnetoconductance shows that the oscillation period depends solely on the parallel component of the applied field [Fig. 4(b)]. We emphasize that the oscillations are observed only in these insulating samples, but not in other more conducting nanotubes. To the best of our knowledge, magnetoconductance oscillations with such large amplitude have not been reported in any other highly insulating systems.

To explore the physical origin of the oscillations, we first recall the origins of quantum conductance oscillations in a normal-metal ring [28]. In the clean limit, the oscillations are due to the Aharonov-Bohm (AB) effect [29], with an oscillation period of h/e, coming from the phase-coherent interference between clockwise- and counterclockwise-traveling electron waves in the ballistic regime. In the diffusive limit with disorders, oscillations with a period of $h/2e$ arise from the Altshuler-Aronov-Spivak (AAS) effect [30], resulting from the interference between time-reversed loops of electrons. Both kinds of oscillation require the phase coherence length to be comparable to the ring circumference. In topological insulator nanostructures, at a zero magnetic field, the surface states will open up an energy gap due to quantum confinement. The conductance oscillations are predicted to arise from the appearance of a gapless surface mode when half-integer fluxes are enclosed by the surface of the system. Since these oscillations have a period of h/e, the same as the AB effect, they are often referred to as the "anomalous AB oscillations" [10,11]. By extracting the area of the inserted flux that is responsible for the oscillation period, we can explore the origin of the observed oscillations. Here we take the nanotube A with a period of 3.53 ± 0.20 kOe as an example. Considering $\Delta B = (0.5 \text{ or } 1)\phi_0/\pi r^2$ where $\phi_0 = h/e$ is the flux quantum, this period corresponds to a diameter of 122 ± 1.8 nm for h/e oscillations, or a diameter of 86.5 ± 2.5 nm for $h/2e$ oscillations. High-resolution FESEM images on the nanotube A show the average outer diameter to be 125 nm, suggesting that the observed oscillations are consistent with the h/e oscillations associated with the outer surface of the nanotube. The AAS effect is ruled out as being responsible for the main oscillations because the corresponding area is much smaller than the cross-sectional areas of either the outer or the inner surface.

Besides the main oscillation period, smaller conductance peaks are also observed in the data. These peaks may come from the AAS oscillation of the outer surface states. However, we cannot determine the period of the smaller peaks and thus we cannot definitively attribute these to AAS oscillations. Normal AB oscillations from bulk carriers are also unlikely to be the cause of the observed oscillations, because the bulk is highly resistive with a short bulk localization length <10 nm. We are not aware of AB oscillation in any other insulating

systems with such a short coherence length. Moreover, the average wall thickness of the nanotube is 13 nm, which is much larger than the surface state penetration length of Bi_2Te_3 obtained by ARPES measurements [31]. If the electron waves responsible for the observed oscillations were distributed through the entire nanotube wall, the period would have a higher value due to the shorter mean center diameter of the bulk. Finally, the average inner diameter is estimated to be 100 nm for the nanotube A and the corresponding oscillation period is approximately 5.28 kOe. From our data, we cannot clearly resolve oscillations with this period. It is tempting to attribute some smaller peaks in the conductance oscillations in Figs. 3 and 4(a) to the inner surface, but the signal is much weaker than the principal oscillations [32]. This could be due to the relatively large roughness of the inner surface of the nanotubes, as expected from the outward diffusion growth process. Therefore, based on the analysis of the oscillation period, we conclude that the main peaks in the conductance oscillations are from the anomalous AB oscillation of the outer surface of the nanotube.

The amplitude of the oscillations decays as the magnetic field increases. We attribute the decay of the oscillation amplitude to a combination of several effects. First, the difference between the maximum and the minimum diameter along the nanotube is estimated to be within 10 nm by measuring at ten positions along the measurement channel. As shown explicitly by the theoretical calculations below, a variation of the diameter of the nanotube causes a broadening of conductance peaks and also smears out the coherence effect as the magnetic field increases. Second, our simulations show that the localization length itself goes down with increasing magnetic fields. Finally, the surface states have a finite penetration length, and thus are subject to a magnetic field that goes through their wave function and breaks time-reversal symmetry.

The fast Fourier transform amplitude of the oscillations is plotted in Fig. 5(a). It follows a $T^{-1/2}$ dependence. For AB or AAS oscillations, this behavior implies the absence of inelastic phonon scattering [28], indicating a phase coherence length larger than the sample diameter. On the other hand, the effective coherence length in the bulk is very short in these nanotubes due to disorder. Therefore, the long coherence length responsible for the oscillations gives additional evidence for the oscillations originating from the surface states.

The magnetoresistance of the nanotubes was also measured in the perpendicular magnetic field direction. Figure 5(b) shows the magnetoresistance of the nanotube B in both perpendicular and parallel fields. Strong anisotropy is observed as expected. In previous reports on Bi_2Te_3 [9] and Bi_2Se_3 [8,33] under a perpendicular magnetic field, a sharp dip in the magnetoresistance appears near the zero field. This effect was attributed to the weak-antilocalization (WAL) effect [34], a quantum interference effect in systems with strong spin-orbit coupling. However, on the Bi_2Te_3 nanotubes, we did not observe this feature. Instead, the magnetoresistance is rather linear in the field range of the measurement (up to 8 T). If we still consider this as the WAL dip, the dip is rather shallow and broad. For nanowires [9], the sample was considered to be in the one-dimensional regime due to the long phase coherence length compared to the wire dimension. In our nanotube samples, the phase coherence length of the bulk is largely affected by disorder, which strongly depresses the quantum correction of weak antilocalization. If we fit the magnetoresistance using the Hikami-Larkin-Nagaoka (HLN) formula for the WAL effect in a 2D system, a short coherence length of ~32 nm is obtained [see Fig. 5(c)]. In fact, we have made the WAL fitting for more than five samples, and all show phase coherence lengths in the range of 30–80 nm. This is one order of magnitude smaller than the reported results in other TI samples which are typically over 300 nm [9,33]. When comparing the estimated phase coherence length and the localization length, one can see that the former is slightly longer than the latter. This means that, as carriers are hopping from site to site, they lose their phase coherence in just one jump, or in successive hops assisted by long-wavelength acoustic phonons [35]. This further confirms the presence of high disorder in the bulk of the nanotubes. The obtained phase coherence length is short compared with the nanotube diameter, and thus the nanotubes can be treated as a rolled 2D sheet. Furthermore, since only a small part of the nanotube walls is perpendicular to the field, the rest contributes very little to the WAL interference. This can also be a contributing factor for the shallow and broad dip in the the magnetoresistance.

It should be pointed out that the R-T analysis indicates that the bulk channel is in the strong-disorder regime and described by the Mott VRH model, while the theory of the weak-(anti)localization effect is developed in the diffusive regime [34]. Therefore, the estimated short phase coherence

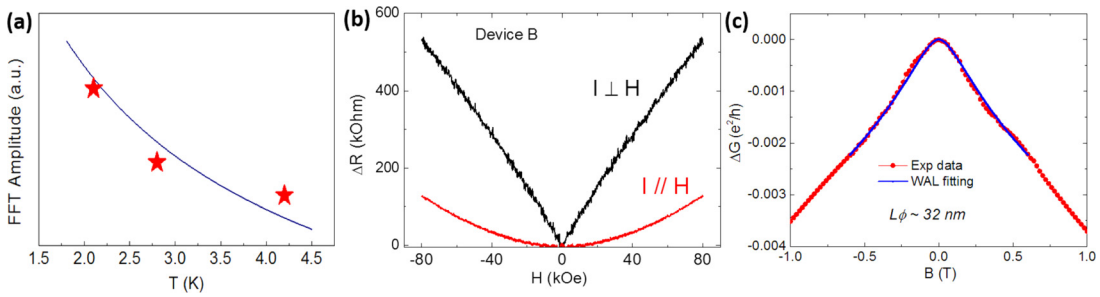

FIG. 5. (a) Temperature dependence of FFT amplitude of the conductance oscillations. It is seen that the data points generally follow a $T^{-1/2}$ trend. (b) Comparison of magnetoresistance in parallel and perpendicular magnetic fields. (c) Fitting of magnetoconductance with weak-antilocalization (WAL) theory. The fitting yields a very short coherence length, which may due to the irrelevance of the formula in a strongly disordered system or because the nanotube geometry is not a real 2D sheet perpendicular to the applied field.

length is neither exactly the right physical quantity nor the right formula in the current system. Nevertheless, the estimated short coherence length supports the notion that the system is in the strong-disorder regime.

Another possible interpretation of the positive magnetoresistance is the linear magnetoresistance due to linear dispersion. The linear magnetoresistance was first proposed by Abrikosov [36] to interpret the unusual magnetoresistance observed in nonstoichiometric silver chalcogenides. Linear magnetoresistance was also observed in topological thin films due to the linear dispersion of surface states [37,38]. Thus, it is natural to expect that positive linear magnetoresistance also occurs in our topological insulator nanotubes. Furthermore, recent studies have shown that linear magnetoresistance can exist even at room temperature [37], suggesting that it is insensitive to dephasing, and thus compatible with the Mott VRH model. The existence of linear magnetoresistance also indicates the importance of surface states with linear dispersion in the transport under magnetic fields.

IV. THEORETICAL MODEL AND ANALYSIS

To gain further insight into the experimental observations, we have performed extensive numerical simulations on transport in TI nanostructures at zero temperature. We consider a widely used four-band model on a simple cubic lattice for TIs with the Hamiltonian [39]

$$H = H_0 + H_{\rm soc} + H_{\rm dis},$$

$$H_0 = \sum_i \left(\varepsilon C_i^\dagger \Gamma_0 C_i - t \sum_\delta (C_{i+\delta}^\dagger \Gamma_0 C_i + C_{i-\delta}^\dagger \Gamma_0 C_i) \right), \quad (1)$$

$$H_{\rm soc} = iA \sum_{i,\delta} (C_{i+\delta}^\dagger \Gamma_i C_i - C_{i-\delta}^\dagger \Gamma_i C_i),$$

$$H_{\rm dis} = \sum_i U_i C_i^\dagger C_i, \quad (2)$$

where $i = (i_x, i_y, i_z)$ denotes lattice sites of a 3D cubic lattice and δ denotes the nearest neighbor. U_i is the random on-site potential at the site i with the potential strength in the range $[-W, W]$ to simulate disorder. The Γ matrices are defined as $\Gamma_x = s_z \otimes \sigma_x$, $\Gamma_y = -I \otimes \sigma_y$, $\Gamma_z = s_x \otimes \sigma_x$, $\Gamma_0 = I \otimes \sigma_z$, where σ_i acts in the orbital space and s_i acts on the spin space. Here a is the lattice constant and set to unity. The material dependent parameters t, A, and ε are chosen to be $\varepsilon = 4t, t = 1, A = 1$ in our calculations. The choice of the parameter is in the range of $2t < |\varepsilon| < 6t$ to realize the strong topological insulator phase [40] and gives a maximum bulk band gap of $4t$.

To focus on understanding the behavior of surface states in the extremely disordered system, we consider a nanowire rather than a nanotube for technical convenience. We study a nanowire with an $N \times N$ square cross section with $N = 9$ and evaluate conductance using the Landauer-Buttiker formalism combined with the iterative Green function method as a function of flux ϕ through the cross section. Our numerical results discussed below are qualitatively independent of the size of the cross section, as confirmed by calculations for $N = 9$ and $N = 8$. The semi-infinite metallic leads are described by the Hamiltonian H_0, and the corresponding Green function is given by [41,42]

$$g^L(y,z,y',z') = \sum_\nu \chi_\nu \tilde{g}^L \chi_\nu, \quad (3)$$

where $\chi_\nu = (1/N_\nu)\sin(k_y y)\sin(k_z z)$ and $\tilde{g}^L = I \otimes (1/t) \begin{pmatrix} -e^{ik_\nu a} & 0 \\ 0 & e^{-ik_\nu a} \end{pmatrix}$. Here $N_\nu = \sum_{yz} \sin^2(k_y y)\sin^2(k_z z)$ is a normalization factor and k_y, k_z are wave vectors quantized in units of $\pi/(N+1)$. The conductance is evaluated using the Landauer-Buttiker formalism $G = (e^2/h){\rm Tr}[\Gamma_L G^r_{1,N+1} \Gamma_R G^a_{1,N+1}]$, in which $G^{r(a)}_{1,N+1}$ is the retarded (advanced) Green function that connects the left and the right ends of the system, and $\Gamma_L = it^2(g^L - g^{L\dagger})$, $\Gamma_R = \Gamma_L^\dagger$ is the coupling to the left and right leads, respectively [42]. The Green functions are evaluated by the recursive Green function method [41]. The localization length λ can be extracted from the Green functions by $1/\lambda = -\lim_{L\to\infty}(1/2L)\ln|G^r_{1,N+1}|^2$ [43]. To simulate the magnetic field B applied along the wire (the x direction), we choose the Landau gauge for the vector potential $\vec{A} = (0, -Bz, 0)$, corresponding to an additional phase factor in the hopping term along the y direction of $(tC^\dagger_{i_y+1} C_{i_y} \to te^{(i2\pi z\phi/\phi_0)} C^\dagger_{i_y+1} C_{i_y})$.

We first look at the energy dispersions of nanowires, which are qualitatively different for integer and half-integer values of magnetic flux measured in units of flux quantum $\phi_0 = h/e$. In the clean limit, there is an energy gap for integer values of ϕ_0, and a gapless Dirac band for half-integer values, as seen, for example, in Fig. 6(a). When the Fermi level is located at the position where several other bands are occupied, the system is metallic for both integer and half-integer fluxes. However, these two cases behave dramatically differently when disorder is introduced. Figure 6(b) shows the dependence of the conductance on the length L of the system for a fixed random disorder. This clearly demonstrates vastly different localization lengths for these two cases. The conductance for $\phi = 0$ is dominated by nontopological carriers and drops exponentially as $\sim e^{-L/\lambda_{\rm non}}$ with the localization length $\lambda_{\rm non} = 150a$ for $W = 2.8$, $E_f = 0.6$. For $\phi = \phi_0/2$, the gapless surface modes show a much longer localization length $\lambda_{\rm top} = 4800a$, which is larger than $\lambda_{\rm non}$ by one order of magnitude and indicates their topological robustness (subscripts refer to "nontopological" and "topological."). It should be emphasized that nontopological carriers for TI nanowires also come from 2D surface states, which are quantized into various 1D modes within the bulk band gap. For a pure bulk system with periodical boundary conditions, the localization length is only around one lattice constant a. The existence of carriers with different localization lengths is consistent with the temperature dependence of resistance in experiments as described above. Different localization lengths for nontopological and topological carriers imply three different regimes for transport in TI nanostructures: (I) $\lambda_{\rm non}, \lambda_{\rm top} > L$, (II) $\lambda_{\rm non} < L < \lambda_{\rm top}$, and (III) $\lambda_{\rm non}, \lambda_{\rm top} < L$. We evaluate the phase diagram explicitly [Fig. 6(c)] as a function of Fermi energy E_f and disorder strength W for a 9×9 system of length $L = 100a$; the qualitative features of the phase diagram should remain valid for arbitrary L although the details will change. In the region I, the conductance shows multiple oscillations coming from both topological

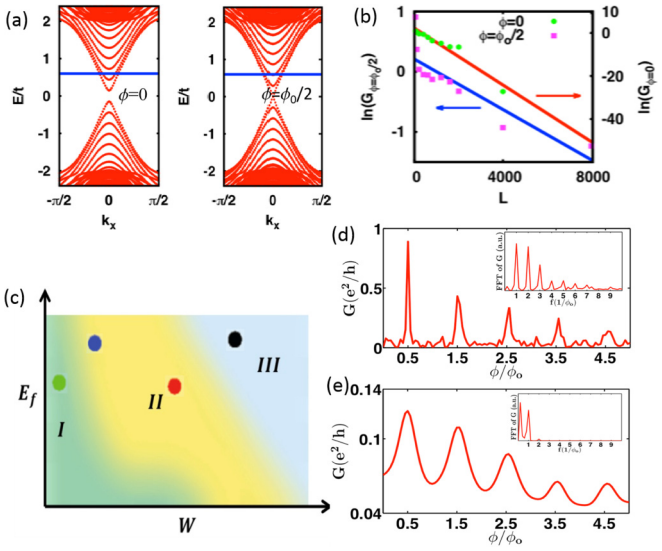

FIG. 6. (a) Band dispersions for a disorder-free system are shown for $\phi = 0$ and $\phi = \phi_0/2$. The solid blue line marks the Fermi energy at $E_f = 0.6$, which is used for the calculations in (b), (c), (d), and (e). (b) Length dependence of the conductance is shown for $\phi = 0$ and $\phi = \phi_0/2$ with $W = 2.8$ and $E_f = 0.6$. The solid lines are linear fits, from which we can extract the localization lengths to be $\lambda_{\rm non} = 150a$ for $\phi = 0$ and $\lambda_{\rm top} = 4800a$ for $\phi = \phi_0/2$. (c) The schematic phase diagram for $L = 100a$. It includes three different regions, denoted as (I) $\lambda_{\rm non}, \lambda_{\rm top} > L$, (II) $\lambda_{\rm non} < L < \lambda_{\rm top}$, and (III) $\lambda_{\rm non} < \lambda_{\rm top} < L$. (d) The magnetoconductance oscillations as a function of magnetic flux ϕ in region II for $W = 2.8$, $L = 800a$, and $E_f = 0.6$. (e) The magnetoconductance oscillations for a system with variations in the cross-sectional area along the length of the nanotube. The cross section is taken to be $9a \times 9a$ for all calculations.

and nontopological bands. In the region III, the conductance is exponentially suppressed and does not show any periodic oscillations. These two regions will be discussed later. Here we focus on the more experimentally relevant region II, where well-defined oscillations with period h/e appear. As shown in Fig. 6(d), the sharp peaks for the magnetic flux $\phi = (n + \frac{1}{2})\phi_0$ indicate that only gapless topological surface modes contribute to transport in this region. This behavior is consistent with the experimental observation that the conductance oscillations do not appear in metallic samples, but only in insulating samples, in which nontopological states are localized and transport is dominated by topological carriers. The peaks observed in experiments are not as sharp as those in our calculations. We believe the rounding arises from variation in the experimental sample of the cross-sectional area along the length of the nanotube, which translates into a distribution for the enclosed magnetic flux. We model the fluctuations in the magnetic flux with a Lorentzian distribution $L_\phi(\xi) = (1/\pi)\{\Gamma/[\Gamma^2 + (\xi - \phi)^2]\}$ where Γ, ϕ is the average magnetic flux and ξ is the variable flux. The average conductance obtained with $\bar{G}(\phi) = \int_0^{5\phi_0} d\xi\ L_\phi(\xi) G(\xi) d\xi$, with $\Gamma = 0.5\phi_0$, is shown in Fig. 6(e), and qualitatively resembles the experimental behavior. If the variations of the cross section are sufficiently large, they can suppress the oscillations altogether, which we believe to be the case with the oscillations associated with topological carriers at the inner surface of the nanotube.

In the region II where the surface state dominates transport, we expect a resistance maximum at $\phi = 0$, which we have confirmed in our simulations. In the region I (or near the crossover boundary between the regions I and II), the situation is more complex, and whether the conductance shows a minimum or a maximum at a zero field depends on parameters such as the Fermi level and the disorder strength [10]. Experimentally, the nanotube B with larger resistance indeed shows a resistance maximum at $\phi = 0$ [Fig. 4(a)], consistent with our expectation. In contrast, the nanotube A shows a resistance minimum (Fig. 3), suggesting that it may lie near the region I.

To complete our discussion, we will next analyze the conductance oscillations for various values of Fermi energy and disorder strength in other regions in the whole phase diagram. We focus on the parameter values represented by the green, blue, red, and black dots in the phase diagram of Fig. 6(c) based on the calculation of the sample size $L = 100a$. In the region I ($L < \lambda_{\rm top}, \lambda_{\rm non}$), we present conductance as a function of inserted flux in Fig. 7(a), where E_f and W are depicted as the green point in Fig. 6(c). In this region, one can see multiple oscillation behaviors. To identify the oscillation period, we take the fast Fourier transform of the conductance, as shown in the inset of Fig. 7(a), from which one can see a main peak, corresponding to oscillation frequency $(1/\phi_0)$, as well as multiple small peaks for higher harmonics with the frequency n/ϕ_0, where n is an integer. The main peak corresponds to the case when the surface carrier, on encircling the perimeter, gains a phase of $2\pi\phi/\phi_0 + \pi$, where the contribution of π arises from the Berry phase. In the weak-disorder limit, the surface carriers can encircle the perimeter multiple times before leaving the nanowire. The phase gained by encircling the perimeter n times is $n \times (2\pi\phi/\phi_0 + \pi)$, and thus addition oscillations with the period h/ne can exist. When E_f and W are chosen in region II but near the boundary with region I [the blue dots in Fig. 6(c)], higher harmonic oscillations are suppressed and only AB-dominant oscillations are observed, as shown in Fig. 7(b) and its inset. This is because the scattering rate increases and consequently the probability of surface carriers circling the perimeter more than once while maintaining phase coherence decreases. Figures 6(d) and 6(e) also correspond to this region, but for $L = 800a$. There are more different behaviors in the region II. Figure 7(c) and the inset show evidence for the Altshuler-Aronov-Spivak (AAS) oscillation. When the system becomes diffusive, the phase difference between two time-reversed paths needs to be taken into account. The phase difference between the clockwise and counterclockwise paths is $2 \times 2\pi\phi/\phi_0$. Therefore, the oscillation period is $h/2e$ [10,11]. In the region III [Fig. 7(d)], where extremely strong disorder is considered or the Fermi energy is so high that bulk carriers dominate the transport, no obvious oscillations can be identified.

Another nontrivial effect of disorder is to produce the so-called topological Anderson insulator, in which an ordinary metal (with a positive gap) is driven into a topological insulator by disorder [39,44,45]. That physics is not relevant here because our system has an inverted band gap even in the absence of disorder. However, it would be worth exploring whether our method for producing highly disordered systems can suggest ways of experimentally realizing topological

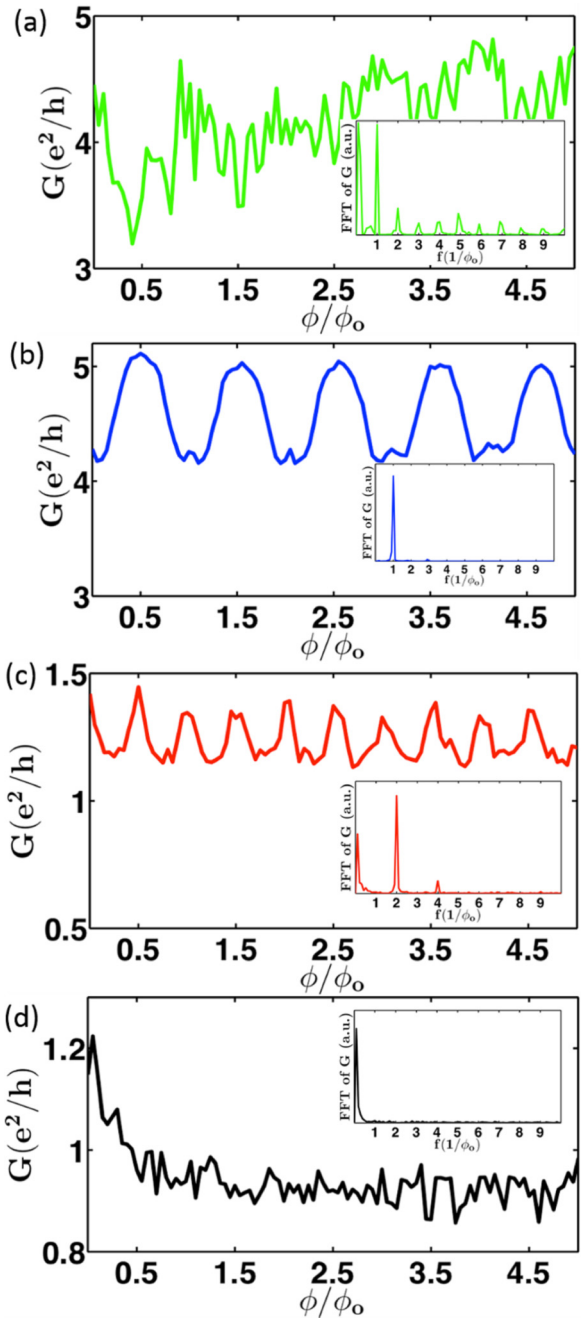

FIG. 7. Theoretical analysis. (a), (b), (c), and (d) correspond to the green, blue, red, and black points in the phase diagram of Fig. 6(c). (a) AB oscillation and its higher harmonics at $W = 0.2, E_f = 0.8$. (b) AB oscillation at $W = 0.8, E_f = 1.3$. (c) AAS oscillation at $W = 2.4, E_f = 0.8$. (d) No oscillation at $W = 3.6, E_f = 1.3$. Insets are the FFTs of corresponding conductance oscillations.

Anderson insulators starting from materials with positive but small band gaps.

V. DISCUSSION

We perform further analysis on the temperature dependence of conductance, and provide more detailed information showing that the bulk channel conductance is strongly suppressed by high disorder, leaving surface states solely responsible for the observed quantum oscillations. The conductance as a function of temperatures can be fitted by the Mott variable range hopping model [25–27] plus a constant for temperatures larger than ∼50 K (Fig. 2 inset), expressed as

$$G(T) = G_C + G_0 \exp\left[-\left(\frac{T}{T_0}\right)^{-1/(d+1)}\right] \tag{4}$$

where T_0 is an energy scale associated with the hopping potential, and d is the effective dimension of the system. The fitting parameters are given as $G_C \sim 4.23\times10^{-5}$ S, $G_0 \sim 1.56\times10^{-3}$ S, $d \sim 2$, and $T_0 \sim 450$ meV. One may also notice that G_C, the temperature-independent conductance channel, has a value very close to one conductance quantum e^2/h. Since the topological surface state conductance is almost temperature independent in this temperature range and should have the conductance value of one conductance quantum, we attribute the constant conductance to the surface states' conduction. The temperature-dependent conduction in this temperature range should come from the bulk channel, which is characterized by the Mott VRH model due to the extremely high disorder.

If we extend the fitting formula to temperatures below 50 K, the experimental data begin to deviate from the fitting formula, as shown in Fig. 8(a). The main reason is that the surface states' conductance decreases with decreasing temperature at low temperatures as reported in Bi_2Se_3 films grown by molecular beam epitaxy (MBE) [22,46]. This was explained as the result of increasing electron-electron interaction [47]. If we subtract the bulk conductance using the Mott VRH expression from the total conductance in the whole temperature range, the remaining surface state conductance clearly behaves very similarly to the reported behavior as shown in Fig. 8(b). For a better comparison, the surface conductance of the nanotube A is plotted together with the data from Ref. [22] for Bi_2Se_3 epitaxial thin films. It is seen that the two curves behave qualitatively similarly and both have values close to one conductance quantum, which corresponds to a single quantum conductance channel. The nanotube surface state conductance is slightly smaller than that of the MBE film. This is not surprising as the nanotube has a strong disorder in the bulk which also affects the surface states as shown in our simulations, while the Bi_2Se_3 MBE film was metallic in the bulk, in the clean regime.

Using the fitting parameters of the Mott VRH model, we can estimate the localization length of the bulk channel. Mott VRH theory gives

$$T_0 \approx \frac{3}{k_B N(E_F) a^2} \tag{5}$$

where a is the localization length and $N(E_F)$ is the 2D density of states at the Fermi level. By using the density of states and the effective mass in the valence band ($0.024m_0$ and $0.134m_0$, where m_0 is the electron rest mass) from a first-principles calculation [48], the 2D density of states is expressed as

$$N_{2D} = \frac{4\pi g\sqrt{m_x m_y}}{h^2} \tag{6}$$

where g is the valley degeneracy. Bulk Bi_2Te_3 has six ellipsoids. In 2D systems, the g factor may be smaller due to lower symmetry [49]. Therefore, the 2D density of states

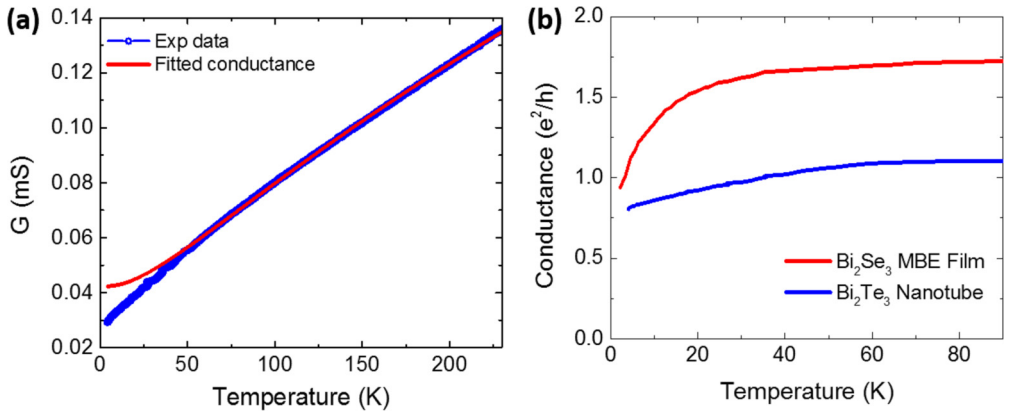

FIG. 8. (a) The fitted conductance (with the VRH model plus a constant) extended to temperatures below 50 K and the measured conductance. (b) The surface channel conductance obtained by subtracting the bulk conductance (VRH) from the total conductance. Surface conductance of Bi_2Se_3 MBE-grown films from Ref. [22] is shown for comparison.

is estimated to be on the order of 10^{14} $eV^{-1}\,cm^{-2}$, which results in a localization length on the order of 1 to 10 nm. It is slightly smaller than the grain size (10–50 nm) observed in the nanotubes from the TEM and SEM studies. There are clearly more scattering centers in the nanotubes than just the grain boundaries, for instance, those caused by the nanotubes being exposed to air during the contact fabrication process, and also by further damage during the FIB process. We want to point out that the effective dimension of 2 from the VRH fitting is reasonable since the estimated localization length is on the order of the nanotube wall thickness, while much smaller than either the circumference or the length of the nanotubes. Therefore, the samples in a hollow nanotube geometry can be treated as a rolled-up thin film.

To further inspect the validity of the dimension 2, the 2D density of states and the carrier concentration are compared by considering charge carriers occupying the subbands due to quantum confinement. The subband energies are given by

$$E(n) = -\frac{h^2 n^2}{8 m_z t^2} \tag{7}$$

where $t \sim 13$ nm is the nanotube wall thickness and n represents the index of the subband. The effective mass $m_z = 1.921\ m_0$ is adopted from first-principle calculations [48]. We obtained $E(n) = E(1)\times n^2 = -1.16\times n^2$ meV. The number of filled subbands is determined by

$$p(\epsilon) = \sum_{n=1}^{\infty} [|\epsilon - E(n)|] N_{2D} \Theta[|\epsilon - E(n)|] \tag{8}$$

where $\Theta(x)$ is the step function. The 2D carrier concentration of the nanotube is $p_{2D} \sim 7.41\times 10^{12}$ cm^{-2}. By setting $p(\epsilon) = p_{2D}$, the Fermi energy is obtained to be -27.2 meV, which is between $E(4) = -18.6$ meV and $E(5) = -29.0$ meV. This means that sub-bands with $n \leqslant 4$ are occupied. We define the occupation percentage of total charge carriers in one specific subband as ρ_n where n labels the subband index. The occupation of each subband is obtained as $\rho_1 = 0.352$, $\rho_2 = 0.305$, $\rho_3 = 0.226$, and $\rho_4 = 0.117$.

Although the bulk channel, the wall of the nanotube, can be treated as a 2D system, the thickness is still large enough so that the outer and inner surface states are well decoupled. According to ARPES measurements on Bi_2Te_3 thin films [31], the surface Dirac cone starts to build up with film thickness greater than 2 quintuple layers (QLs). This suggests that the penetration length of surface states on Bi_2Te_3 is about 1 nm. Considering that the bulk gap of $Bi_2Te_3 \sim 200$ meV, a simple estimation gives the coupling strength as $t \sim 0.2\ \exp(-13/1)$ eV $\sim 4\times 10^{-4}$ meV, which is well below our measurement temperature. Furthermore, since the areas enclosed by the outer surface and inner surface are different, it is unlikely that approximate time-reversal symmetry will be present for both inner and outer surfaces simultaneously with an applied magnetic field during measurements. This means that, when the outer surface is gapless, the inner one may have a gap, the size of which is estimated to be 2 meV for a 50 nm radius and much larger than the coupling strength. Therefore, no hybridization is expected between surface states at the inner and outer surfaces.

As we pointed out earlier, only on those insulating nanotubes have we observed the anomalous AB oscillations. On the other metallic nanotubes, since the bulk channel has lower disorder, the nanotube conduction is dominated by the non-topological trivial states, and as a result, topological surface states are shortened and no signatures like the anomalous AB effect can show up.

VI. SUMMARY

In summary, we have studied topological insulator Bi_2Te_3 nanotubes with carrier concentration that is similar to those in previously reported metallic samples, but with a sufficiently strong disorder that freezes out bulk conduction. We have observed quantum oscillations in magnetoconductance with a period that can be attributed to the outer surface states. The experimental results and the simulations verify a fundamental aspect of the three-dimensional topological insulators, namely, that the surface states are robust against strong disorder.

ACKNOWLEDGMENT

The authors would like to acknowledge the partial support from the Department of Energy (DOE) Grant No. DE-FG02-08ER46531 (Q.L.) for experimental studies, DOE Grant No. DE-SC0005042 (A.C.B.) and Office of Naval Research

under the Grant No. N00014-15-1-2675 (C.X.L.) for theoretical studies, National Science Foundation Grant No. DMR-1207474 (Q.L.) National Natural Science Foundation of China and NBPRC Grant No. 2012CB922003 (X.L.) for nanotube growth, and the partial student support from the Penn State Materials Research Science and Engineering Center, funded by the National Science Foundation under Grants No. DMR-0820404 and No. DMR-1420620 (M.C.).

R.Z.D. conducted nanofabrication and measurements; H-C.H., A.C.B., J.K.J., and C.X.L. conducted theoretical calculations; D.K. and S.T. conducted thermal transport measurements; Y.Y. and S.D. grew the nanotubes, W.D., W.Z., S-Y. Y., and J.W. assisted in the experiments; R.Z.D., H-C.H., J.K.J., C.X.L., and Q.L. were responsible for drafting the manuscript; S.E.M., S.T., X.L., N.S., and M.H.M.C. contributed to the discussion and revision of the manuscript. Q.L. was responsible for the design, planning, and supervision of the overall experimental work; J.K.J. and C.X.L. were responsible for the planning and supervision of the theoretical work.

Renzhong Du and Hsiu-Chuan Hsu contributed equally to this work.

[1] C. L. Kane and E. J. Mele, Phys. Rev. Lett. **95**, 146802 (2005).
[2] B. A. Bernevig and S.-C. Zhang, Phys. Rev. Lett. **96**, 106802 (2006).
[3] L. Fu, C. Kane, and E. Mele, Phys. Rev. Lett. **98**, 106803 (2007).
[4] Y. Xia, D. Qian, D. Hsieh, L. Wray, A. Pal, H. Lin, A. Bansil, D. Grauer, Y. S. Hor, R. J. Cava, and M. Z. Hasan, Nature Phys. **5**, 398 (2009).
[5] Y. Zhang, K. He, C. Z. Chang, C. L. Song, L. L. Wang, X. Chen, J. F. Jia, Z. Fang, X. Dai, W. Y. Shan, S. Q. Shen, Q. Niu, X. L. Qi, S. C. Zhang, X. C. Ma, and Q. K. Xue, Nature Phys. **6**, 584 (2010).
[6] H. Peng, K. Lai, D. Kong, S. Meister, Y. Chen, X. L. Qi, S. C. Zhang, Z. X. Shen, and Y. Cui, Nature Mater. **9**, 225 (2010).
[7] F. Xiu, L. He, Y. Wang, L. Cheng, L. T. Chang, M. Lang, G. Huang, X. Kou, Y. Zhou, X. Jiang, Z. Chen, J. Zou, A. Shailos, and K. L. Wang, Nature Nanotechnol. **6**, 216 (2011).
[8] D. Zhang, J. Wang, A. M. DaSilva, J. S. Lee, H. R. Gutierrez, M. H. W. Chan, J. Jain, and N. Samarth, Phys. Rev. B **84**, 165120 (2011).
[9] M. L. Tian, W. Ning, Z. Qu, H. F. Du, J. Wang, and Y. H. Zhang, Sci. Rep. **3**, 1212 (2013).
[10] J. H. Bardarson, P. W. Brouwer, and J. E. Moore, Phys. Rev. Lett. **105**, 156803 (2010).
[11] Y. Zhang and A. Vishwanath, Phys. Rev. Lett. **105**, 206601 (2010).
[12] G. Q. Zhang, Q. X. Yu, and X. G. Li, Dalton T **39**, 993 (2010).
[13] F. Seitz, J. Phys. Soc. Jpn. **10**, 679 (1955).
[14] See Supplemental Material at http://link.aps.org/supplemental/10.1103/PhysRevB.93.195402 for more details of the Bi_2Te_3 nanotube synthesis and charaterizations.
[15] N. B. Duarte, Ph.D. thesis, The Pennsylvania State University, 2008.
[16] J. Krumrain, G. Mussler, S. Borisova, T. Stoica, L. Plucinski, C. M. Schneider, and D. Grützmacher, J. Cryst. Growth **324**, 115 (2011).
[17] X. Liu, D. J. Smith, J. Fan, Y. H. Zhang, H. Cao, Y. P. Chen, J. Leiner, B. J. Kirby, M. Dobrowolska, and J. K. Furdyna, Appl. Phys. Lett. **99**, 171903 (2011).
[18] Y. S. Hor, D. Qu, N. P. Ong, and R. J. Cava, J. Phys.: Condens. Matter **22**, 115 (2010).
[19] See Supplemental Material at http://link.aps.org/supplemental/10.1103/PhysRevB.93.195402 for the estimation of carrier concentration from Seebeck coefficient measurements.
[20] J. E. Brom, Y. Ke, R. Z. Du, D. Won, X. J. Weng, K. Andre, J. C. Gagnon, S. E. Mohney, Q. Li, K. Chen, X. X. Xi, and J. M. Redwing, Appl. Phys. Lett. **100**, 162110 (2012).
[21] K. Eto, Z. Ren, A. A. Taskin, K. Segawa, and Y. Ando, Phys. Rev. B **81**, 195309 (2010).
[22] Y. S. Kim, M. Brahlek, N. Bansal, E. Edrey, G. A. Kapilevich, K. Iida, M. Tanimura, Y. Horibe, S.-W. Cheong, and S. Oh, Phys. Rev. B **84**, 073109 (2011).
[23] J. Wang, H. D. Li, C. Z. Chang, K. He, J. S. Lee, H. Z. Lu, Y. Sun, X. C. Ma, N. Samarth, S. Q. Shen, Q. K. Xue, M. H. Xie, and M. H. W. Chan, Nano Res. **5**, 739 (2012).
[24] L. He, F. X. Xiu, X. X. Yu, M. Teague, W. J. Jiang, Y. B. Fan, X. F. Kou, M. R. Lang, Y. Wang, G. Huang, N. C. Yeh, and K. L. Wang, Nano Lett. **12**, 1486 (2012).
[25] N. F. Mott, J Non-Cryst. Solids **1**, 1 (1968).
[26] F. R. Allen and C. J. Adkins, Philos. Mag. **26**, 1027 (1972).
[27] W. N. Shafarman and T. G. Castner, Phys. Rev. B **33**, 3570 (1986).
[28] S. Washburn, C. P. Umbach, R. B. Laibowitz, and R. A. Webb, Phys. Rev. B **32**, 4789 (1985).
[29] Y. Aharonov and D. Bohm, Phys. Rev. **115**, 485 (1959).
[30] B. L. Altshuler, A. G. Aronov, and B. Z. Spivak, JETP Lett. **33**, 94 (1981).
[31] Y. Y. Li, G. A. Wang, X. G. Zhu, M. H. Liu, C. Ye, X. Chen, Y. Y. Wang, K. He, L. L. Wang, X. C. Ma, H. J. Zhang, X. Dai, Z. Fang, X. C. Xie, Y. Liu, X. L. Qi, J. F. Jia, S. C. Zhang, and Q. K. Xue, Adv. Mater. **22**, 4002 (2010).
[32] See Supplemental Material at http://link.aps.org/supplemental/10.1103/PhysRevB.93.195402 for the analysis of oscillations from nanotube inner surface.
[33] J. J. Cha, M. Claassen, D. S. Kong, S. S. Hong, K. J. Koski, X. L. Qi, and Y. Cui, Nano Lett. **12**, 4355 (2012).
[34] S. Hikami, A. I. Larkin, and Y. Nagaoka, Prog. Theor. Phys. **63**, 707 (1980).
[35] F. Tremblay, M. Pepper, D. Ritchie, D. C. Peacock, J. E. F. Frost, and G. A. C. Jones, Phys. Rev. B **39**, 8059 (1989).
[36] A. A. Abrikosov, Phys. Rev. B **58**, 2788 (1998).
[37] X. L. Wang, Y. Du, S. X. Dou, and C. Zhang, Phys. Rev. Lett. **108**, 266806 (2012).
[38] H. T. He, B. K. Li, H. C. Liu, X. Guo, Z. Y. Wang, M. H. Xie, and J. N. Wang, Appl. Phys. Lett. **100**, 032105 (2012).
[39] H. M. Guo, G. Rosenberg, G. Refael, and M. Franz, Phys. Rev. Lett. **105**, 216601 (2010).
[40] G. Rosenberg and M. Franz, Phys. Rev. B **82**, 035105 (2010).
[41] C. H. Lewenkopf and E. R. Mucciolo, J. Comput. Electron. **12**, 203 (2013).

[42] S. Datta, *Electronic Transport in Mesoscopic Systems*, Cambridge Studies in Semiconductor Physics and Microelectronic Engineering Vol. 3 (Cambridge University Press, Cambridge, 1995).
[43] B. Kramer and A. Mackinnon, Rep. Prog. Phys. **56**, 1469 (1993).
[44] J. Li, R. L. Chu, J. K. Jain, and S. Q. Shen, Phys. Rev. Lett. **102**, 136806 (2009).
[45] C. W. Groth, M. Wimmer, A. R. Akhmerov, J. Tworzydlo, and C. W. J. Beenakker, Phys. Rev. Lett. **103**, 196805 (2009).
[46] M. H. Liu, C. Z. Chang, Z. C. Zhang, Y. Zhang, W. Ruan, K. He, L. L. Wang, X. Chen, J. F. Jia, S. C. Zhang, Q. K. Xue, X. C. Ma, and Y. Y. Wang, Phys. Rev. B **83**, 165440 (2011).
[47] J. Wang, A. M. DaSilva, C. Z. Chang, K. He, J. K. Jain, N. Samarth, X. C. Ma, Q. K. Xue, and M. H. W. Chan, Phys. Rev. B **83**, 245438 (2011).
[48] B. Y. Yavorsky, N. F. Hinsche, I. Mertig, and P. Zahn, Phys. Rev. B **84**, 165208 (2011).
[49] L. D. Hicks and M. S. Dresselhaus, Phys. Rev. B **47**, 12727 (1993).